Multi-port Network Modeling and Stability Analysis of VSC-MTDC Systems

Shangning Tan, Junliang Liu, Xiong Du, *Member*, *IEEE*, Jingyuan Su, and Lijuan Fan

***Abstract*—The voltage source converter based multi-terminal high-voltage direct current (VSC-MTDC) system has attracted much attention because it can achieve the interconnection between AC grids. However, the initial phases and short-circuit ratios (SCRs) of the interconnected AC grids cause the steady-state phases (SSPs) of AC ports in the VSC-MTDC system to be different. This can lead to issues such as mismatches in multiple converter reference frame systems, potentially causing inaccuracies in stability analysis when this phenomenon is disregarded. To address the aforementioned issues, a multi-port network model of the VSC-MTDC system, which considers the SSPs of the AC grids and AC ports, is derived by multiplying the port models of different subsystems (SSs). The proposed multi-port network model can accurately describe the transmission characteristics between the input and output ports of the system. Additionally, this model facilitates accurate analysis of the system stability. Furthermore, it identifies the key factors affecting the system stability. Ultimately, the accuracy of the proposed multi-port network model and the analysis of key factors are verified by time-domain simulations.**

***Index Terms*—Normalized sensitivity, multi-port network model, steady-state phase, small-signal stability, voltage source converter based multi-terminal high-voltage direct current (VSC-MTDC).**

I. Introduction

THE voltage source converter based multi-terminal high-voltage direct current (VSC-MTDC) systems play an essential role in achieving the interconnection between non-synchronous AC grids, especially when there are differences in the initial phases and short-circuit ratios (SCRs) of these grids [1], [2]. However, the interaction between the VSC-MTDC system and the AC grids may lead to system instability, affecting the safe and stable operation of AC grids [1]-[3]. Therefore, it is necessary to study the stability of the VSC-MTDC system.

The time-domain simulation model can analyze the system stability, but it cannot provide the theoretical support to identify key factors that cause instability [4]. The analytical model used to analyze stability overcomes this problem. At present, the analytical model is divided into two major categories: modal models [5], [6] and impedance models [7]-[10]. The impedance model has been widely used for the VSC-MTDC system [7]-[10].

References [9]-[12] establish the simplified impedance models of the VSC-MTDC system, which may lead to inaccurate stability analysis since it ignores the coupling characteristics [13]. In [14]-[16], the detailed single-input single-output (SISO) impedance models of the system are established through the iteration of subsystems (SSs). However, it is necessary to determine the right-half-plane (RHP) pole in the equivalent models to accurately analyze the system stability [17], [18]. To avoid the potential instability issues arising from RHP cancellation, multiple SISO SS models are used to analyze and evaluate the RHP pole of the system layer by layer [19]. When the system control parameters change, it is necessary to re-iterate the calculation to obtain the SISO impedance model and RHP poles, which is complex for the study of large-scale systems [16]. Therefore, the SISO impedance model based on one port is inefficient for analyzing the stability of large-scale systems.

The multiple-input multiple-output (MIMO) impedance model based on traditional two-port network has difficulty in reflecting the multi-frequency interaction characteristics of the AC and DC ports for voltage source converter (VSC) [20]. The MIMO impedance models describing the interaction between the AC and DC ports of VSCs are established in the *dq* frame and *αβ* frame [21]-[27]. The third-order admittance matrix models of the VSC and the VSC-MTDC system in the *dq* frame are also established [21], [22]. However, these models ignore the coordinate matching between multiple VSCs. To address this concern, a hybrid AC/DC admittance model for the stability assessment of the multi-terminal DC transmission system is established in [25], where the system stability is assessed and three instability root causes are identified. Moreover, [26] develops a frequency-domain admittance network model considering the overall dynamics of hybrid AC/DC systems with modular multilevel converters (MMCs) and proposes a novel frequency-domain criterion to quantify the oscillatory stability. Furthermore, an index called DC interaction factor (DCIF) is proposed, which facilitates determining whether to treat a hybrid AC/DC system separately or simultaneously without loss of accu-

Manuscript received: September 7, 2023; revised: December 18, 2023; accepted: February 20, 2024. Date of CrossCheck: February 20, 2024. Date of online publication: April 23, 2024.

This work was supported by the National Natural Science Key Foundation of China (No. 51937001) and in part by the Fundamental Research Funds for the Central Universities (No. 2023CDJXY-029).

This article is distributed under the terms of the Creative Commons Attribution 4.0 International License (http://creativecommons.org/licenses/by/4.0/).

S. Tan, J. Liu (corresponding author), X. Du, and J. Su are with School of Electrical Engineering, Chongqing University, Chongqing, China (e-mail: tsn@cqu.edu.cn; ljl@cqu.edu.cn; duxiong@cqu.edu.cn; sujingyuan@cqu.edu.cn).

L. Fan is with the CSG Electric Power Research Institute, China Southern Power Grid, Guangzhou, China (e-mail: fanlj03@163.com).

DOI: 10.35833/MPCE.2023.000648

racy. However, they ignore the steady-state phases (SSPs) of AC ports, which causes inaccurate stability analysis.

To address the above issues, a multi-port network model considering the SSPs of AC ports in the VSC-MTDC system is formulated by combining the port models of SSs through multiplication. The key contributions are listed below.

1) The multi-port network model of VSC-MTDC system can be obtained by multiplying the port transmission parameter matrices of SSs.

2) The proposed multi-port network model considers SSPs of AC ports in the VSC-MTDC system, which accurately characterizes the transmission characteristics between the input and output ports of the system.

3) The key factors affecting the system stability are identified, thereby providing a theoretical foundation for designing stability improvement strategies in the VSC-MTDC system.

The rest of this paper is organized as follows. Section II establishes a multi-port network model of a VSC-MTDC system. In Section III, the accuracy of the proposed multi-port network model and the system stability analysis are verified by case studies. The key factors affecting the stability of the VSC-MTDC system are located, and the analysis accuracy is verified by MATLAB/Simulink in Section IV. Finally, Section V concludes the research work.

II. Multi-port Network Model of VSC-MTDC System

In this section, the VSC-MTDC system is divided into three SSs: VSCs, DC network, and AC grids. The port models of the three SSs considering the SSPs of AC ports are established. A generalized two-port network model to characterize multi-frequency components of the VSC is proposed. The multi-port network model, describing the transmission characteristics between the input and output ports of the VSC-MTDC system, is obtained by multiplying the port models of the three SSs. The specific formulation of the multi-port model for the VSC-MTDC system is detailed in this section.

A. Structure of VSC-MTDC System

The structure of a VSC-MTDC system is shown in Fig. 1(a). The DC network and the AC grids of the VSC-MTDC system can adopt any topological structure. V_i^g and θ_i are the steady-state voltage amplitude and phase of the i^{th} AC grid, respectively; V_i^{ac} and I_i^{ac} are the steady-state amplitudes of the voltage and current for the AC port of the i^{th} VSC, respectively; θ_{vi} and θ_{ii} are the steady-state phases of the voltage and current for the AC port of the i^{th} VSC, respectively; and V_i^{dc} and I_i^{dc} are the steady-state voltage and current for DC port of the i^{th} VSC, respectively. In the rectifier terminal, $i=1,2,\ldots,m$; and in the inverter terminal, $i=n,n+1,\ldots,j$.

For Fig. 1(a), the SSPs of AC ports of various grid-connected VSCs may be different because of the various SCRs and initial phases of AC grids, which make the *dq* frames of multiple VSCs be different, as shown in Fig. 1(b). This leads to the mismatch in the reference frames of system.

Therefore, the zero phase is set as the unified reference frame. The phase of any AC grid can be selected as a zero phase reference, and in this paper, the phase of the 1st AC grid θ_1 is selected, as shown in the red dashed line in Fig. 1(b). The black solid lines and the blue dashed lines are the $\alpha\beta$ frames and *dq* frames of the VSCs ignoring the SSPs.

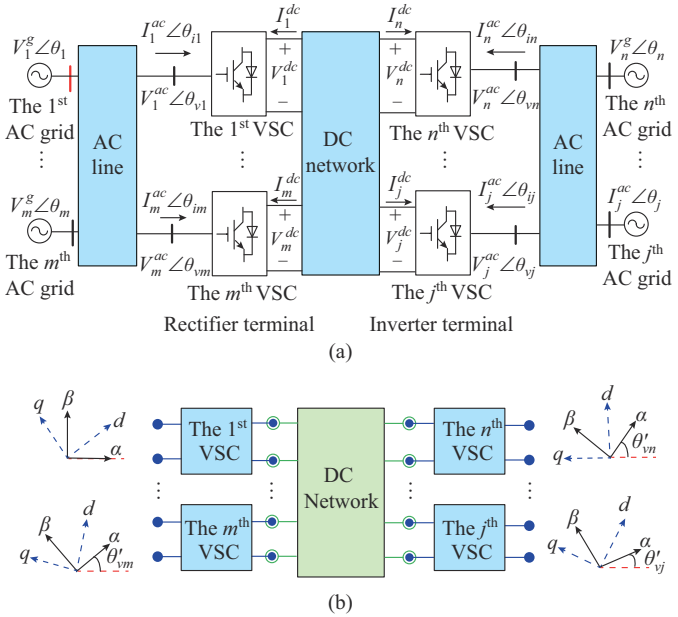

Fig. 1. Structure of VSC-MTDC system. (a) Structure of VSC-MTDC system. (b) Port network model considering SSPs of AC port.

B. Port Model of VSC

The main circuit of a VSC in the unified $\alpha\beta$ frame is shown in Fig. 2. The VSC includes an AC port and a DC port. With two frequency interactions, the AC port of VSC has small-signal voltage and current models with two frequencies (denoted by s and $s-2\mathrm{j}\omega_1$) [4]. $V_{\mathrm{u},i}^{\alpha\beta}(s)$ and $V_{\mathrm{u},i}^{\alpha\beta}(s-2\mathrm{j}\omega_1)$ are the small-signal voltages for the AC prot of the i^{th} VSC in the unified $\alpha\beta$ frame; $I_{\mathrm{u},i}^{\alpha\beta}(s)$ and $I_{\mathrm{u},i}^{\alpha\beta}(s-2\mathrm{j}\omega_1)$ are the small-signal currents for the AC prot of the i^{th} VSC in the unified $\alpha\beta$ frame; $V_i^{dc}(s-\mathrm{j}\omega_1)$ and $I_i^{dc}(s-\mathrm{j}\omega_1)$ are the small-signal DC voltage and current of the i^{th} VSC in the united $\alpha\beta$ frame, respectively; $V_{\mathrm{u},i}^{m\alpha\beta}(s)$ is the voltage of AC line connected with the i^{th} VSC in the unified $\alpha\beta$ frame; $\omega_1=2\pi f_1$ is the fundamental angular frequency; and L and R are the inductance and resistance of the AC filter, respectively. In this paper, the superscript $\alpha\beta$ represents the values in the $\alpha\beta$ frame; and the subscript u represents the values in the unified frame.

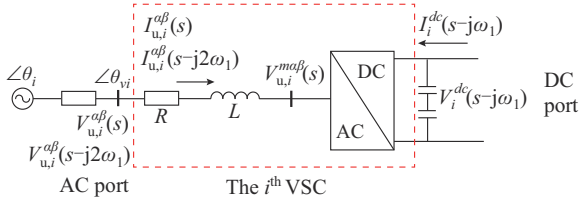

Fig. 2. Main circuit of VSC in unified $\alpha\beta$ frame.

When the initial phase of the AC port of VSC is 0, the three-phase steady-state voltages for the AC port of the i^{th} VSC in the $\alpha\beta$ frame can be expressed as (1) and that in the

dq frame can be obtained by Park transformation.

$$V_i^{ac}\mathrm{e}^{\mathrm{j}\omega_1 t}\xrightarrow{\text{Park transformation}}V_i^{ac} \tag{1}$$

The steady-state voltage amplitudes of the AC port are the same in different coordinate systems. The currents and duty cycles of the AC port can be obtained in a similar way.

The phase offset for the AC port of the i^{th} VSC θ'_{vi} caused by the grid impedance can be expressed as:

$$\theta'_{vi}=\theta_{vi}-\theta_1 \tag{2}$$

At this time, the Park transformation of the small-signal voltage for the AC port of the i^{th} VSC can be expressed as:

$$\begin{cases} V_{\mathrm{u},i}^{\alpha\beta}(s)=V_i^{\alpha\beta}(s)\mathrm{e}^{\mathrm{j}\theta'_{vi}} \\ V_{\mathrm{u},i}^{dq}(s-\mathrm{j}\omega_1)=V_i^{dq}(s-\mathrm{j}\omega_1)\mathrm{e}^{\mathrm{j}\theta'_{vi}} \end{cases} \tag{3}$$

$$V_{\mathrm{u},i}^{\alpha\beta}(s)\xrightarrow{\text{Park transformation}}V_{\mathrm{u},i}^{dq}(s-\mathrm{j}\omega_1) \tag{4}$$

where the superscript *dq* represents the values in the *dq* frame; and $V_i^{\alpha\beta}(s)$ and $V_i^{dq}(s-\mathrm{j}\omega_1)$ are the small-signal voltages for the AC port of the i^{th} VSC in the *αβ* frame and *dq* frame without considering the SSPs of the AC port, respectively. The above phase conversion relationship of coordinate system is also applicable to the small-signal models of the currents and duty cycles of the AC port.

The steady-state electrical parameters of the DC ports are scalars, and there is no deviation in the SSPs.

Based on the structure in Fig. 2, the small-signal voltages and currents for the AC port of the i^{th} VSC can be obtained by:

$$\begin{bmatrix} V_{\mathrm{u},i}^{m\alpha\beta}(s) \\ \left(V_{\mathrm{u},i}^{m\alpha\beta}(\mathrm{j}2\omega_1-s)\right)^* \\ I_{\mathrm{u},i}^{m\alpha\beta}(s) \\ \left(I_{\mathrm{u},i}^{m\alpha\beta}(\mathrm{j}2\omega_1-s)\right)^* \end{bmatrix}=\boldsymbol{G}_{acf}\boldsymbol{M}_\theta\begin{bmatrix} V_{\mathrm{u},i}^{\alpha\beta}(s) \\ \left(V_{\mathrm{u},i}^{\alpha\beta}(\mathrm{j}2\omega_1-s)\right)^* \\ I_{\mathrm{u},i}^{\alpha\beta}(s) \\ \left(I_{\mathrm{u},i}^{\alpha\beta}(\mathrm{j}2\omega_1-s)\right)^* \end{bmatrix} \tag{5}$$

$$\boldsymbol{G}_{acf}=\begin{bmatrix} 1 & 0 & sL+R & 0 \\ 0 & 1 & 0 & (s-2\mathrm{j}\omega_1)L+R \\ 0 & 0 & 1 & 0 \\ 0 & 0 & 0 & 1 \end{bmatrix} \tag{6}$$

$$\boldsymbol{M}_\theta=\begin{bmatrix} \mathrm{e}^{-\mathrm{j}\theta'_{vi}} & 0 & 0 & 0 \\ 0 & \mathrm{e}^{\mathrm{j}\theta'_{vi}} & 0 & 0 \\ 0 & 0 & \mathrm{e}^{-\mathrm{j}\theta'_{vi}} & 0 \\ 0 & 0 & 0 & \mathrm{e}^{\mathrm{j}\theta'_{vi}} \end{bmatrix} \tag{7}$$

where $\boldsymbol{G}_{acf}$ represents the relationship between the input and output electrical parameters of AC filter for the VSC; $\boldsymbol{M}_\theta$ represents the phase offsets of the AC port caused by the grid impedances; $I_{\mathrm{u},i}^{m\alpha\beta}(s)$ is the current of the AC line connected with the i^{th} VSC in the unified *αβ* frame; and * is the symbol of conjugate.

The minor voltage perturbation in the AC port of VSC induces a disturbance in the output phase of the phase-locked loop (PLL). At this time, the AC voltages and currents in the *αβ* frame are transformed by Park transformation to obtain the AC voltages and currents in the *dq* frame. Based on the control structure of PLL, a small-signal model for the output phase of PLL can be obtained [12]. Therefore, the relationship of the voltages and currents for the AC port of the i^{th} VSC between the unified *αβ* frame and *dq* frame can be derived as:

$$\begin{bmatrix} V_{\mathrm{u},i}^{dq}(s-\mathrm{j}\omega_1) \\ \left(V_{\mathrm{u},i}^{dq}(\mathrm{j}\omega_1-s)\right)^* \\ I_{\mathrm{u},i}^{dq}(s-\mathrm{j}\omega_1) \\ \left(I_{\mathrm{u},i}^{dq}(\mathrm{j}\omega_1-s)\right)^* \end{bmatrix}=\boldsymbol{G}_{pll}^{ui}\boldsymbol{M}_\theta\begin{bmatrix} V_{\mathrm{u},i}^{\alpha\beta}(s) \\ \left(V_{\mathrm{u},i}^{\alpha\beta}(\mathrm{j}2\omega_1-s)\right)^* \\ I_{\mathrm{u},i}^{\alpha\beta}(s) \\ \left(I_{\mathrm{u},i}^{\alpha\beta}(\mathrm{j}2\omega_1-s)\right)^* \end{bmatrix} \tag{8}$$

$$\boldsymbol{G}_{pll}^{ui}=\begin{bmatrix} 1-0.5V_i^{ac}T_{pll}(s-\mathrm{j}\omega_1) & 0 & 0 & 0 \\ 0 & 0.5V_i^{ac}\left(T_{pll}(\mathrm{j}\omega_1-s)\right)^* & 0 & 0 \\ -0.5I_i^{ac}T_{pll}(s-\mathrm{j}\omega_1) & 0 & 0 & 0 \\ 0 & 0.5I_i^{ac}\left(T_{pll}(\mathrm{j}\omega_1-s)\right)^* & 0 & 0 \end{bmatrix} \tag{9}$$

where $T_{pll}(s)$ is the closed-loop transfer function of PLL.

Similarly, the relationship of duty cycles D of the i^{th} VSC between the unified *αβ* frame and *dq* frame can be derived as:

$$\begin{bmatrix} D_{\mathrm{u},i}^{\alpha\beta}(s) \\ \left(D_{\mathrm{u},i}^{\alpha\beta}(\mathrm{j}2\omega_1-s)\right)^* \\ 0 \\ 0 \end{bmatrix}=\boldsymbol{M}_d\begin{bmatrix} D_{\mathrm{u},i}^{dq}(s-\mathrm{j}\omega_1) \\ \left(D_{\mathrm{u},i}^{dq}(\mathrm{j}\omega_1-s)\right)^* \\ 0 \\ 0 \end{bmatrix}+\boldsymbol{G}_{pll}^{d}\boldsymbol{M}_\theta\begin{bmatrix} V_{\mathrm{u},i}^{\alpha\beta}(s) \\ \left(V_{\mathrm{u},i}^{\alpha\beta}(\mathrm{j}2\omega_1-s)\right)^* \\ I_{\mathrm{u},i}^{\alpha\beta}(s) \\ \left(I_{\mathrm{u},i}^{\alpha\beta}(\mathrm{j}2\omega_1-s)\right)^* \end{bmatrix} \tag{10}$$

$$\boldsymbol{G}_{pll}^{d}=0.5D_i^{ac}\begin{bmatrix} -T_{pll}(s-\mathrm{j}\omega_1) & 0 & 0 & 0 \\ 0 & \left(T_{pll}(\mathrm{j}\omega_1-s)\right)^* & 0 & 0 \\ 0 & 0 & 0 & 0 \\ 0 & 0 & 0 & 0 \end{bmatrix} \tag{11}$$

$$\boldsymbol{M}_d=\begin{bmatrix} \mathrm{e}^{-\mathrm{j}\theta'_{vi}} & 0 & 0 & 0 \\ 0 & \mathrm{e}^{\mathrm{j}\theta'_{vi}} & 0 & 0 \\ 0 & 0 & 0 & 0 \\ 0 & 0 & 0 & 0 \end{bmatrix} \tag{12}$$

where D_i^{ac} is the steady-state duty cycle of the i^{th} VSC.

The AC and DC active power of VSC is conserved when the internal loss of VSC is ignored. The relationship of the small-signal voltage and current between the AC and DC ports of the i^{th} VSC can be described as:

$$\begin{bmatrix} V_i^{dc}(s-\mathrm{j}\omega_1)/2 \\ \left(V_i^{dc}(\mathrm{j}\omega_1-s)\right)^*/2 \\ -I_i^{dc}(s-\mathrm{j}\omega_1)/2 \\ \left(-I_i^{dc}(\mathrm{j}\omega_1-s)\right)^*/2 \end{bmatrix}=\boldsymbol{G}_1\begin{bmatrix} V_{\mathrm{u},i}^{\alpha\beta}(s) \\ \left(V_{\mathrm{u},i}^{\alpha\beta}(\mathrm{j}2\omega_1-s)\right)^* \\ I_{\mathrm{u},i}^{\alpha\beta}(s) \\ \left(I_{\mathrm{u},i}^{\alpha\beta}(\mathrm{j}2\omega_1-s)\right)^* \end{bmatrix}+\boldsymbol{G}_2\begin{bmatrix} D_{\mathrm{u},i}^{\alpha\beta}(s) \\ \left(D_{\mathrm{u},i}^{\alpha\beta}(\mathrm{j}2\omega_1-s)\right)^* \\ 0 \\ 0 \end{bmatrix} \tag{13}$$

$$\boldsymbol{G}_1=\begin{bmatrix} \dfrac{1}{D_i^{ac}} & 0 & 0 & 0 \\ 0 & \dfrac{1}{\left(D_i^{ac}\right)^*} & 0 & 0 \\ 0 & 0 & \dfrac{3D_i^{ac}}{2} & \dfrac{3\left(D_i^{ac}\right)^*}{2} \\ 0 & 0 & \dfrac{3\left(D_i^{ac}\right)^*}{2} & \dfrac{3D_i^{ac}}{2} \end{bmatrix} \tag{14}$$

$$\boldsymbol{G}_2=\begin{bmatrix} \dfrac{V_i^{dc}}{D_i^{ac}} & 0 & 0 & 0 \\ 0 & \dfrac{V_i^{dc}}{\left(D_i^{ac}\right)^*} & 0 & 0 \\ \dfrac{3I_i^{ac}}{2} & \dfrac{3\left(I_i^{ac}\right)^*}{2} & 0 & 0 \\ \dfrac{3\left(I_i^{ac}\right)^*}{2} & \dfrac{3I_i^{ac}}{2} & 0 & 0 \end{bmatrix} \tag{15}$$

The block diagram of DC voltage control for VSC is shown in Appendix A Fig. A1. If the VSC controls AC current, the relationship between the duty cycle of VSC and its voltage and current in the unified *dq* frame is described as:

$$\boldsymbol{M}_d\begin{bmatrix} D_{\mathrm{u},i}^{dq}\left(s-\mathrm{j}\omega_1\right) \\ \left(D_{\mathrm{u},i}^{dq}\left(\mathrm{j}\omega_1-s\right)\right)^* \\ 0 \\ 0 \end{bmatrix}=\left(\boldsymbol{G}_i+\boldsymbol{G}_{dep}\right)\boldsymbol{G}_p\boldsymbol{M}_\theta\begin{bmatrix} V_{\mathrm{u},i}^{dq}\left(s-\mathrm{j}\omega_1\right) \\ \left(V_{\mathrm{u},i}^{dq}\left(\mathrm{j}\omega_1-s\right)\right)^* \\ I_{\mathrm{u},i}^{dq}\left(s-\mathrm{j}\omega_1\right) \\ \left(I_{\mathrm{u},i}^{dq}\left(\mathrm{j}\omega_1-s\right)\right)^* \end{bmatrix} \tag{16}$$

$$\boldsymbol{G}_i=\begin{bmatrix} 0 & 0 & -H_i\left(s-\mathrm{j}\omega_1\right) & 0 \\ 0 & 0 & 0 & \left(-H_i\left(\mathrm{j}\omega_1-s\right)\right)^* \\ 0 & 0 & 0 & 0 \\ 0 & 0 & 0 & 0 \end{bmatrix} \tag{17}$$

$$\boldsymbol{G}_{dep}=\begin{bmatrix} 0 & 0 & -\mathrm{j}\omega_1 L & 0 \\ 0 & 0 & 0 & \mathrm{j}\omega_1 L \\ 0 & 0 & 0 & 0 \\ 0 & 0 & 0 & 0 \end{bmatrix} \tag{18}$$

$$\boldsymbol{G}_p=\begin{bmatrix} 0 & 0 & 0 & 0 \\ 0 & 0 & 0 & 0 \\ 0 & 0 & 1/V_i^{dc} & 0 \\ 0 & 0 & 0 & 1/V_i^{dc} \end{bmatrix} \tag{19}$$

where $\boldsymbol{G}_i$ represents the proportional-integral (PI) control of AC current; $\boldsymbol{G}_{dep}$ represents the decoupling of the current control; $\boldsymbol{G}_p$ represents the modulation of the VSC; and $H_i(s)$ represents the PI control of current.

The small-signal model for the sampling of VSC is expressed as:

$$\boldsymbol{G}_f=\begin{bmatrix} G_f(s) & 0 & 0 & 0 \\ 0 & \left(G_f\left(\mathrm{j}2\omega_1-s\right)\right)^* & 0 & 0 \\ 0 & 0 & G_f(s) & 0 \\ 0 & 0 & 0 & \left(G_f\left(\mathrm{j}2\omega_1-s\right)\right)^* \end{bmatrix} \tag{20}$$

where $G_f(s)=1/\left(1+sT_s\right)$, and T_s is the sampling period.

When the DC port of VSC is the output port and the AC port is the input port, the inverse transmission parameter model of the VSC can be derived based on (5)-(20):

$$\begin{bmatrix} V_i^{dc}(s-\mathrm{j}\omega_1) \\ \left(V_i^{dc}\left(\mathrm{j}\omega_1-s\right)\right)^* \\ -I_i^{dc}\left(s-\mathrm{j}\omega_1\right) \\ \left(-I_i^{dc}\left(\mathrm{j}\omega_1-s\right)\right)^* \end{bmatrix}=\boldsymbol{T}_i^L\begin{bmatrix} V_{\mathrm{u},i}^{\alpha\beta}(s) \\ \left(V_{\mathrm{u},i}^{\alpha\beta}\left(\mathrm{j}2\omega_1-s\right)\right)^* \\ I_{\mathrm{u},i}^{\alpha\beta}(s) \\ \left(I_{\mathrm{u},i}^{\alpha\beta}\left(\mathrm{j}2\omega_1-s\right)\right)^* \end{bmatrix} \tag{21}$$

The elements in the inverse transmission parameter matrix $\boldsymbol{T}_i^L$ describe the interaction between small-signal current and voltage of the AC and DC ports for VSC.

When the VSC controls AC current, $\boldsymbol{T}_i^L$ considering the phase offsets caused by the grid impedances can be derived as:

$$\boldsymbol{T}_i^L=\left[\boldsymbol{G}_1\boldsymbol{G}_{acf}+\boldsymbol{G}_2\left(\boldsymbol{G}_i+\boldsymbol{G}_{dep}\right)\boldsymbol{G}_p\boldsymbol{G}_{pll}^{ui}\boldsymbol{G}_f+\boldsymbol{G}_2\boldsymbol{G}_{pll}^{d}\right]\boldsymbol{M}_\theta \tag{22}$$

If the VSC controls the DC voltage, the small-signal model for the PI control of DC voltage is described as:

$$\boldsymbol{G}_v=\begin{bmatrix} H_v\left(s-\mathrm{j}\omega_1\right) & 0 & 0 & 0 \\ 0 & \left(H_v\left(\mathrm{j}\omega_1-s\right)\right)^* & 0 & 0 \\ 0 & 0 & 0 & 0 \\ 0 & 0 & 0 & 0 \end{bmatrix} \tag{23}$$

where $H_v(s)$ represents the PI control of DC voltage.

When the VSC controls the DC voltage, the relationship of the current and voltage between the AC and DC ports of the VSC considering the phase offsets can be derived as:

$$\boldsymbol{T}_i^L=\left[\boldsymbol{G}_1\boldsymbol{G}_{acf}+\boldsymbol{G}_2\left(\boldsymbol{G}_i+\boldsymbol{G}_{dep}\right)\boldsymbol{G}_p\boldsymbol{G}_{pll}^{ui}\boldsymbol{G}_f+\boldsymbol{G}_2\boldsymbol{G}_{pll}^{d}\right]\boldsymbol{M}_\theta\left(\boldsymbol{I}-\boldsymbol{G}_2\boldsymbol{G}_v\boldsymbol{G}_i\boldsymbol{G}_p\boldsymbol{G}_f\right)^{-1} \tag{24}$$

where $\boldsymbol{I}$ is the unit matrix.

C. Conversion of Port Parameter Models

When the DC port of the VSC is the input port and the AC port is the output port, the multi-frequency interaction of the VSC port can be described by the transmission parameter model. The transmission parameter model of the VSC is obtained by the inverse transmission parameter matrix, which is shown as:

$$\begin{bmatrix} V_{\mathrm{u},i}^{\alpha\beta}(s) \\ \left(V_{\mathrm{u},i}^{\alpha\beta}\left(\mathrm{j}2\omega_1-s\right)\right)^* \\ I_{\mathrm{u},i}^{\alpha\beta}(s) \\ \left(I_{\mathrm{u},i}^{\alpha\beta}\left(\mathrm{j}2\omega_1-s\right)\right)^* \end{bmatrix}=\boldsymbol{T}_i\begin{bmatrix} V_i^{dc}\left(s-\mathrm{j}\omega_1\right) \\ \left(V_i^{dc}\left(\mathrm{j}\omega_1-s\right)\right)^* \\ -I_i^{dc}\left(s-\mathrm{j}\omega_1\right) \\ \left(-I_i^{dc}\left(\mathrm{j}\omega_1-s\right)\right)^* \end{bmatrix} \tag{25}$$

$$\boldsymbol{T}_i=\left(\boldsymbol{T}_i^L\right)^{-1} \tag{26}$$

D. Multi-port Models of VSC-MTDC Systems

Compared with the SISO impedance models obtained by node impedance iteration in [16]-[18], the proposed multi-port parameter model is only related to the steady-state values and the internal parameters of the SSs, which realizes the modularization of system modeling. In the VSC-MTDC systems, the power of rectifier-terminal VSCs flows from the AC ports to DC ports, while the power of the inverter-terminal VSCs flows from the DC ports to AC ports.

The inverse transmission parameter model $\boldsymbol{T}_{sr}^L$ describing the interaction between the input ports and the output ports of the rectifier-terminal VSCs can be obtained as:

$$\begin{bmatrix} V_1^{dc}(s-\mathrm{j}\omega_1) \\ \left(V_1^{dc}(\mathrm{j}\omega_1-s)\right)^* \\ \vdots \\ V_m^{dc}(s-\mathrm{j}\omega_1) \\ \left(V_m^{dc}(\mathrm{j}\omega_1-s)\right)^* \\ I_1^{dc}(s-\mathrm{j}\omega_1) \\ \left(I_1^{dc}(\mathrm{j}\omega_1-s)\right)^* \\ \vdots \\ I_m^{dc}(s-\mathrm{j}\omega_1) \\ \left(I_m^{dc}(\mathrm{j}\omega_1-s)\right)^* \end{bmatrix} = \boldsymbol{T}_{sr}^L \begin{bmatrix} V_{\mathrm{u},1}^{\alpha\beta}(s) \\ \left(V_{\mathrm{u},1}^{\alpha\beta}(\mathrm{j}2\omega_1-s)\right)^* \\ \vdots \\ V_{\mathrm{u},m}^{\alpha\beta}(s) \\ \left(V_{\mathrm{u},m}^{\alpha\beta}(\mathrm{j}2\omega_1-s)\right)^* \\ I_{\mathrm{u},1}^{\alpha\beta}(s) \\ \left(I_{\mathrm{u},1}^{\alpha\beta}(\mathrm{j}2\omega_1-s)\right)^* \\ \vdots \\ I_{\mathrm{u},m}^{\alpha\beta}(s) \\ \left(I_{\mathrm{u},m}^{\alpha\beta}(\mathrm{j}2\omega_1-s)\right)^* \end{bmatrix} \tag{27}$$

$$\boldsymbol{T}_{sr}^L=\begin{bmatrix} \boldsymbol{T}_1^L & 0 & \cdots & 0 \\ 0 & \boldsymbol{T}_2^L & \cdots & 0 \\ \vdots & \vdots & & \vdots \\ 0 & 0 & \cdots & \boldsymbol{T}_m^L \end{bmatrix} \tag{28}$$

Based on the topology of DC network in Fig. 1, the transmission parameter model $\boldsymbol{T}_{dcn}$ can be used to describe the characteristics of DC network ports:

$$\begin{bmatrix} V_n^{dc}(s-\mathrm{j}\omega_1) \\ \left(V_n^{dc}(\mathrm{j}\omega_1-s)\right)^* \\ \vdots \\ V_j^{dc}(s-\mathrm{j}\omega_1) \\ \left(V_j^{dc}(\mathrm{j}\omega_1-s)\right)^* \\ I_n^{dc}(s-\mathrm{j}\omega_1) \\ \left(I_n^{dc}(\mathrm{j}\omega_1-s)\right)^* \\ \vdots \\ I_j^{dc}(s-\mathrm{j}\omega_1) \\ \left(I_j^{dc}(\mathrm{j}\omega_1-s)\right)^* \end{bmatrix} = \boldsymbol{T}_{dcn} \begin{bmatrix} V_1^{dc}(s-\mathrm{j}\omega_1) \\ \left(V_1^{dc}(\mathrm{j}\omega_1-s)\right)^* \\ \vdots \\ V_m^{dc}(s-\mathrm{j}\omega_1) \\ \left(V_m^{dc}(\mathrm{j}\omega_1-s)\right)^* \\ -I_1^{dc}(s-\mathrm{j}\omega_1) \\ \left(-I_1^{dc}(\mathrm{j}\omega_1-s)\right)^* \\ \vdots \\ -I_m^{dc}(s-\mathrm{j}\omega_1) \\ \left(-I_m^{dc}(\mathrm{j}\omega_1-s)\right)^* \end{bmatrix} \tag{29}$$

The port transmission parameter model $\boldsymbol{T}_{si}$ describing the interaction between the input ports and the output ports of the inverter-terminal VSCs can be obtained as:

$$\begin{bmatrix} V_{\mathrm{u},n}^{\alpha\beta}(s) \\ \left(V_{\mathrm{u},n}^{\alpha\beta}(\mathrm{j}2\omega_1-s)\right)^* \\ \vdots \\ V_{\mathrm{u},j}^{\alpha\beta}(s) \\ \left(V_{\mathrm{u},j}^{\alpha\beta}(\mathrm{j}2\omega_1-s)\right)^* \\ I_{\mathrm{u},n}^{\alpha\beta}(s) \\ \left(I_{\mathrm{u},n}^{\alpha\beta}(\mathrm{j}2\omega_1-s)\right)^* \\ \vdots \\ I_{\mathrm{u},j}^{\alpha\beta}(s) \\ \left(I_{\mathrm{u},j}^{\alpha\beta}(\mathrm{j}2\omega_1-s)\right)^* \end{bmatrix} = \boldsymbol{T}_{si} \begin{bmatrix} V_n^{dc}(s-\mathrm{j}\omega_1) \\ \left(V_n^{dc}(\mathrm{j}\omega_1-s)\right)^* \\ \vdots \\ V_j^{dc}(s-\mathrm{j}\omega_1) \\ \left(V_j^{dc}(\mathrm{j}\omega_1-s)\right)^* \\ I_n^{dc}(s-\mathrm{j}\omega_1) \\ \left(I_n^{dc}(\mathrm{j}\omega_1-s)\right)^* \\ \vdots \\ I_j^{dc}(s-\mathrm{j}\omega_1) \\ \left(I_j^{dc}(\mathrm{j}\omega_1-s)\right)^* \end{bmatrix} \tag{30}$$

The rectifier-terminal and inverter-terminal VSCs are connected by the DC network to form a multi-port network of the VSC-MTDC system. Based on (27)-(30), the multi-port network model of the VSC-MTDC system can be derived as:

$$\begin{bmatrix} V_{\mathrm{u},n}^{\alpha\beta}(s) \\ \left(V_{\mathrm{u},n}^{\alpha\beta}(\mathrm{j}2\omega_1-s)\right)^* \\ \vdots \\ V_{\mathrm{u},j}^{\alpha\beta}(s) \\ \left(V_{\mathrm{u},j}^{\alpha\beta}(\mathrm{j}2\omega_1-s)\right)^* \\ I_{\mathrm{u},n}^{\alpha\beta}(s) \\ \left(I_{\mathrm{u},n}^{\alpha\beta}(\mathrm{j}2\omega_1-s)\right)^* \\ \vdots \\ I_{\mathrm{u},j}^{\alpha\beta}(s) \\ \left(I_{\mathrm{u},j}^{\alpha\beta}(\mathrm{j}2\omega_1-s)\right)^* \end{bmatrix} = \boldsymbol{T}_{si}\boldsymbol{T}_{dcn}\boldsymbol{T}_{sr}^L \begin{bmatrix} V_{\mathrm{u},1}^{\alpha\beta}(s) \\ \left(V_{\mathrm{u},1}^{\alpha\beta}(\mathrm{j}2\omega_1-s)\right)^* \\ \vdots \\ V_{\mathrm{u},m}^{\alpha\beta}(s) \\ \left(V_{\mathrm{u},m}^{\alpha\beta}(\mathrm{j}2\omega_1-s)\right)^* \\ I_{\mathrm{u},1}^{\alpha\beta}(s) \\ \left(I_{\mathrm{u},1}^{\alpha\beta}(\mathrm{j}2\omega_1-s)\right)^* \\ \vdots \\ I_{\mathrm{u},m}^{\alpha\beta}(s) \\ \left(I_{\mathrm{u},m}^{\alpha\beta}(\mathrm{j}2\omega_1-s)\right)^* \end{bmatrix} \tag{31}$$

When the VSCs and DC network are interconnected by DC ports, the DC ports of both SSs become built-in ports. It is worth noting that (31) still contains the interaction characteristics between the DC ports and the AC ports of VSCs in the VSC-MTDC system.

The relationships between the AC voltages and currents of the AC grids can be derived as:

$$\boldsymbol{M}_g^I \begin{bmatrix} V_{\mathrm{u},n}^{\alpha\beta}(s) \\ \left(V_{\mathrm{u},n}^{\alpha\beta}(\mathrm{j}2\omega_1-s)\right)^* \\ \vdots \\ V_{\mathrm{u},j}^{\alpha\beta}(s) \\ \left(V_{\mathrm{u},j}^{\alpha\beta}(\mathrm{j}2\omega_1-s)\right)^* \\ V_{\mathrm{u},n}^{g}(s) \\ 0 \\ \vdots \\ V_{\mathrm{u},j}^{g}(s) \\ 0 \end{bmatrix} = \boldsymbol{G}_{net}^I \boldsymbol{M}_g^I \begin{bmatrix} V_{\mathrm{u},n}^{\alpha\beta}(s) \\ \left(V_{\mathrm{u},n}^{\alpha\beta}(\mathrm{j}2\omega_1-s)\right)^* \\ \vdots \\ V_{\mathrm{u},j}^{\alpha\beta}(s) \\ \left(V_{\mathrm{u},i}^{\alpha\beta}(\mathrm{j}2\omega_1-s)\right)^* \\ I_{\mathrm{u},n}^{\alpha\beta}(s) \\ \left(I_{\mathrm{u},n}^{\alpha\beta}(\mathrm{j}2\omega_1-s)\right)^* \\ \vdots \\ I_{\mathrm{u},j}^{\alpha\beta}(s) \\ \left(I_{\mathrm{u},j}^{\alpha\beta}(\mathrm{j}2\omega_1-s)\right)^* \end{bmatrix} \tag{32}$$

$$\boldsymbol{G}_{net}^{I}=\begin{bmatrix}\boldsymbol{I} & \boldsymbol{0}\\ \boldsymbol{I} & \boldsymbol{Z}_{net}^{I}\end{bmatrix} \tag{33}$$

$$\boldsymbol{M}_{g}^{I}=\begin{bmatrix}\mathrm{e}^{-\mathrm{j}\theta_n'} & 0 & \cdots & 0 & 0\\ 0 & \mathrm{e}^{\mathrm{j}\theta_n'} & \cdots & 0 & 0\\ \vdots & \vdots & & \vdots & \vdots\\ 0 & 0 & \cdots & \mathrm{e}^{-\mathrm{j}\theta_j'} & 0\\ 0 & 0 & \cdots & 0 & \mathrm{e}^{\mathrm{j}\theta_j'}\end{bmatrix} \tag{34}$$

where $\boldsymbol{Z}_{net}^{I}$ is the grid impedance that connects inverter-terminal VSCs; $\boldsymbol{M}_{g}^{I}$ represents the phase offsets of the AC grids connected to the inverter-terminal VSC in the unified frame; and $\theta_i'=\theta_i-\theta_1$. Similarly, the grid impedance $\boldsymbol{Z}_{net}^{R}$ that connects the rectifier-terminal VSCs and the matrix $\boldsymbol{M}_{g}^{R}$ that represents the phase offsets of the AC grids connected to the rectifier-terminal VSCs in the unified frame can be obtained in the same way.

Based on (31) and (32), the transfer function $\boldsymbol{G}_{sys}^{clo\prime}$ between the small-signal voltages of the AC ports for rectifier-terminal and inverter-terminal VSCs, considering the port phase offsets, can be derived as:

$$\begin{bmatrix}V_{\mathrm{u},n}^{\alpha\beta}(s)\\ \left(V_{\mathrm{u},n}^{\alpha\beta}(\mathrm{j}2\omega_1-s)\right)^{*}\\ \vdots\\ V_{\mathrm{u},j}^{\alpha\beta}(s)\\ \left(V_{\mathrm{u},j}^{\alpha\beta}(\mathrm{j}2\omega_1-s)\right)^{*}\\ V_{\mathrm{u},n}^{g}(s)\\ 0\\ \vdots\\ V_{\mathrm{u},j}^{g}(s)\\ 0\end{bmatrix}=\boldsymbol{G}_{sys}^{clo\prime}\begin{bmatrix}V_{\mathrm{u},1}^{\alpha\beta}(s)\\ \left(V_{\mathrm{u},1}^{\alpha\beta}(\mathrm{j}2\omega_1-s)\right)^{*}\\ \vdots\\ V_{\mathrm{u},m}^{\alpha\beta}(s)\\ \left(V_{\mathrm{u},m}^{\alpha\beta}(\mathrm{j}2\omega_1-s)\right)^{*}\\ V_{\mathrm{u},1}^{g}(s)\\ 0\\ \vdots\\ V_{\mathrm{u},m}^{g}(s)\\ 0\end{bmatrix} \tag{35}$$

where $\boldsymbol{G}_{sys}^{clo\prime}=\left(\boldsymbol{M}_{g}^{I}\right)^{-1}\boldsymbol{G}_{net}^{I}\boldsymbol{M}_{g}^{I}\boldsymbol{T}_{si}\boldsymbol{T}_{dcn}\boldsymbol{T}_{sr}^{L}\boldsymbol{M}_{g}^{R}\left(\boldsymbol{G}_{net}^{R}\right)^{-1}\left(\boldsymbol{M}_{g}^{R}\right)^{-1}$.

III. Validations and Case Studies

To verify the accuracy of the proposed multi-port network model, the port closed-loop gain matrix of VSC-MTDC system is used. A VSC-MTDC system is established in MATLAB/Simulink. The port model of SSs considering the SSPs of AC ports is verified, and the effect of the proposed multi-port network model on the stability analysis of VSC-MTDC system is analyzed by two cases.

A. Case Study

The structure of a four-terminal VSC-MTDC system shown in Fig. 3 is established in MATLAB/Simulink. The parameters are shown in Appendix A Table AI in [13]. The rectifier-terminal VSCs control AC currents, and the inverter-terminal VSCs control DC voltages. The SCRs of AC grids are 3, and phase of the 1st AC grid θ_1 lags 60° than that of other AC grids.

To verify the proposed multi-port network model of the VSC-MTDC system, the rows and columns in (35) can be exchanged to obtain a port closed-loop gain matrix, which can be expressed as:

$$\begin{bmatrix}V_{\mathrm{u},1}^{\alpha\beta}(s)\\ \left(V_{\mathrm{u},1}^{\alpha\beta}(\mathrm{j}2\omega_1-s)\right)^{*}\\ \vdots\\ V_{\mathrm{u},j}^{\alpha\beta}(s)\\ \left(V_{\mathrm{u},j}^{\alpha\beta}(\mathrm{j}2\omega_1-s)\right)^{*}\end{bmatrix}=\boldsymbol{G}_{sys}^{clo}\begin{bmatrix}V_{\mathrm{u},1}^{g}(s)\\ 0\\ \vdots\\ V_{\mathrm{u},j}^{g}(s)\\ 0\end{bmatrix} \tag{36}$$

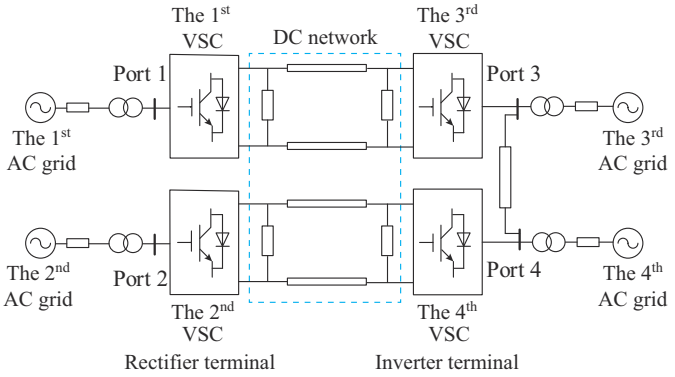

Fig. 3. Structure of a four-terminal VSC-MTDC system.

In MATLAB/Simulink, small voltage disturbances of the AC grids at different frequencies are injected in turn, and then the voltage responses of AC input and output ports are measured.

Figure 4 shows the Bode diagrams of the elements (in the first column) of the port closed-loop gain matrix, where the horizontal axis (frequency) adopts logarithmic coordinates. The simulation measurements of the port closed-loop gain matrix of the VSC-MTDC system are obtained as shown in the red dotted lines. The theoretical model considering SSPs of AC port is expressed as orange dashed lines, and the theoretical model without considering SSPs of AC port is expressed as black solid lines.

It can be observed from Fig. 4(b)-(d) that the theoretical models G_{sys51}^{clo}, G_{sys21}^{clo}, and G_{sys61}^{clo} considering the SSPs of AC port are consistent with the simulation measurement, which verifies the accuracy of the proposed multi-port network model.

B. Stability Analysis Based on Port Network Models

The VSC-MTDC system is stable when connected to ideal AC grids, the proposed multi-port network model in (31) does not include RHP poles.

The open-loop gain model of the system $\boldsymbol{G}_{sys}^{open}$ can be obtained based on the port closed-loop gain matrix to analyze the system stability.

$$\boldsymbol{G}_{sys}^{open}=\left(\boldsymbol{G}_{sys}^{clo}\right)^{-1}-\boldsymbol{I}=\begin{bmatrix}\boldsymbol{G}_{1m}^{RR} & \boldsymbol{G}_{mj}^{RI}\\ \boldsymbol{G}_{jm}^{IR} & \boldsymbol{G}_{nj}^{II}\end{bmatrix} \tag{37}$$

where $\boldsymbol{G}_{1m}^{RR}$ and $\boldsymbol{G}_{nj}^{II}$ are the open-loop gain matrices that characterize the AC ports of the rectifier-terminal and inverter-terminal VSCs, respectively; and $\boldsymbol{G}_{jm}^{IR}$ and $\boldsymbol{G}_{mj}^{RI}$ are the interactive open-loop gain matrices between the AC ports of rectifier-terminal and inverter-terminal VSCs, respectively.

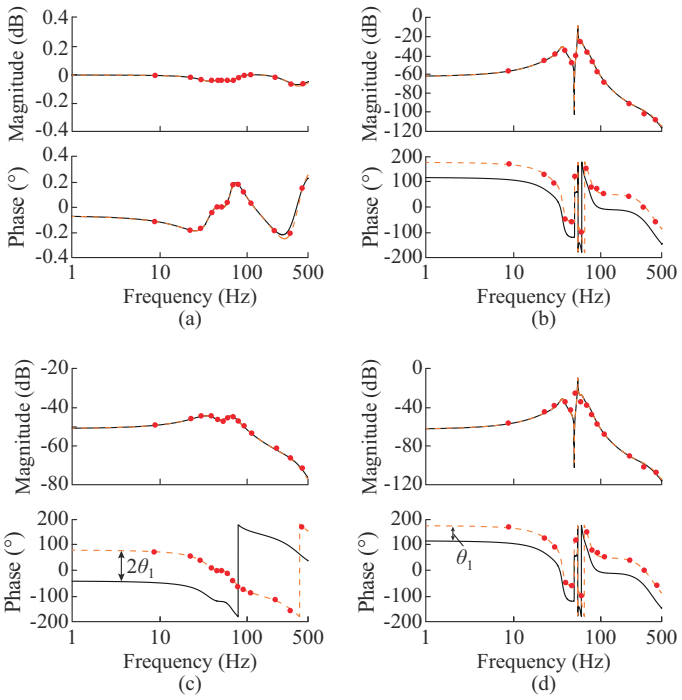

Fig. 4. Bode diagram of elements in port closed-loop gain matrix. (a) G^{clo}_{sys11}. (b) G^{clo}_{sys51}. (c) G^{clo}_{sys21}. (d) G^{clo}_{sys61}.

To facilitate the stability analysis of the system and identify the key factors, the eigenvalues of the system can be expressed as:

$$\left|\boldsymbol{\lambda}+\boldsymbol{G}_{sys}^{open}\right|=\left|\boldsymbol{\lambda}+\boldsymbol{G}_{lm}^{RR}\right|\left|\boldsymbol{\lambda}+\boldsymbol{G}_{ni}^{II}-\boldsymbol{G}_{im}^{IR}\left(\boldsymbol{I}+\boldsymbol{G}_{lm}^{RR}\right)^{-1}\boldsymbol{G}_{mi}^{RI}\right| \quad (38)$$

where $\boldsymbol{\lambda}$ is the vector of eigenvalues.

The eigenvalues λ_1 and λ_2 are associated with the port 1 of the 1st VSC, while λ_3 and λ_4 are associated with the port 2 of the 2nd VSC. If λ_1 or λ_2 encircles the point $(-1,0)$, the 1st VSC is the dominant resonant module. Similarly, if λ_3 or λ_4 encircles the point $(-1,0)$, the 2nd VSC is the dominant resonant module. The same conclusions can be obtained with respect to the 3rd and 4th VSCs when λ_5-λ_8 encircle the point $(-1,0)$. The generalized Nyquist analysis based on the port closed-loop gain matrix can preliminarily screen out the VSC that causes the system instability.

To verify the effect of SSPs of AC port on the stability of the VSC-MTDC system, two cases are analyzed.

1) Case I

In case I, the SCRs of the 1st and 2nd AC grids are 5 and 2.5, respectively. And the SCRs of the 3rd and 4th AC grids are 2.4 and 5, respectively. The initial phases of AC grid voltages are the same, and the SSPs of AC ports are different.

As shown by Nyquist diagrams of system eigenvalues in case I in Fig. 5, the system stability is analyzed with and without considering the SSPs of AC port.

In Fig. 5(a), the eigenvalues λ_1-λ_8 do not encircle the point $(-1,0)$, while in Fig. 5(b), the eigenvalue λ_5 encircles the point (–1, 0) and it means that VSC-MTDC system is unstable, which is consistent with the simulation results in Fig. 6. Hence, the stability analysis results of the proposed multi-port network model considering the SSPs of AC port are more accurate compared with that of the existing port network models without considering the SSPs of AC port.

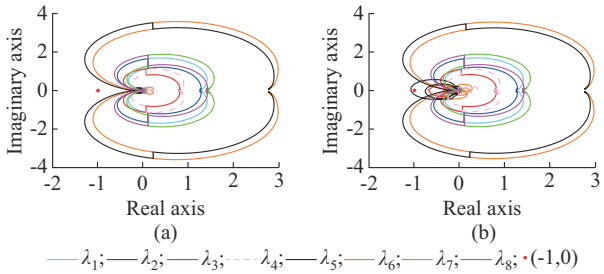

Fig. 5. Nyquist diagrams of system eigenvalues in case I. (a) Without considering SSPs of AC port. (b) Considering SSPs of AC port.

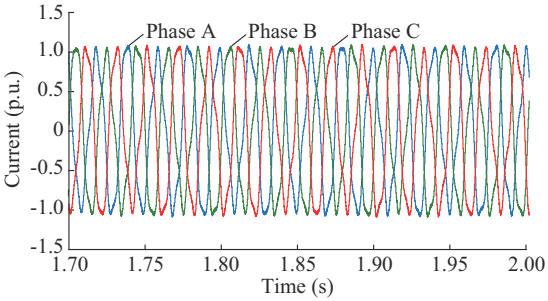

Fig. 6. Simulation diagram of grid current in case I.

2) Case II

In case II, the SCRs of all AC grids are 2.5. The initial phase of the 4th AC grid lags 60° than that of 1st-3rd AC grids.

Figure 7 shows the Nyquist diagrams of system eigenvalues in case II. In Fig. 7(a), the eigenvalues λ_1-λ_8 do not encircle the point $(-1,0)$, while in Fig. 7(b), the eigenvalue λ_7 encircles the point $(-1,0)$ and it means that the system is unstable, which is consistent with the simulation results in Fig. 8. Therefore, when the initial phases of the AC grids are different, the proposed multi-port network model is more accurate in stability analysis than the existing port network models.

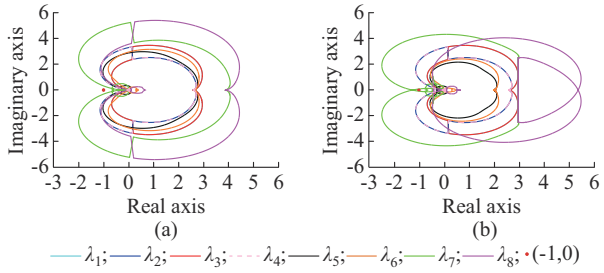

Fig. 7. Nyquist diagram of system eigenvalues in case II. (a) Without considering SSPs of AC port. (b) Considering SSPs of AC port.

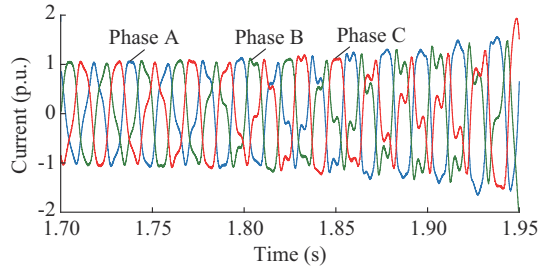

Fig. 8. Simulation diagram of grid current in case II.

Based on the analysis of cases I and II, the proposed multi-port network model considering SSPs of AC port can accurately analyze the stability when the VSC-MTDC system is interconnected with the AC grids that have different SCRs and initial phases.

IV. Key Factor Recognition

To reduce the effect of the SSPs of AC ports on the stability of VSC-MTDC system, the normalized sensitivities between system control parameters and eigenvalues are analyzed and the key factors affecting the system stability are accurately located in this section.

Based on the eigenvalue λ_k encircling the point $(-1,0)$ and the stability laws of a single grid-connected VSC [28], [29], the resonating interfaces that cause the system instability are located. The VSC interconnected with the resonant port is the dominant resonant module [25]. The control parameters that affect the stability of VSC-MTDC system are determined based on the law for the stability of a single VSC and parameters. The normalized sensitivities of the eigenvalue λ_k to the control parameters are calculated. The key factors affecting the system stability can be obtained. The most useful sensitivity information is the normalized sensitivity of eigenvalue (which is near or encloses $(-1,0)$) magnitude to the control parameters. Based on the sensitivity symbol and normalized sensitivity, the control parameters that have the greatest impact on system stability are adjusted, so that the system can quickly achieve the safe and stable operation.

The key factors affecting the system stability are obtained by comparing the normalized sensitivities of eigenvalue magnitude. The sensitivity of the eigenvalue to the control parameter x is expressed as:

$$\hat{S}_x^{\lambda_k(s)} = \lim_{\Delta x \to 0} \frac{\lambda_k(x+\Delta x, f_0) - \lambda_k(x, f_0)}{(x+\Delta x) - x} \tag{39}$$

where f_0 is the shearing frequency; and x is the control parameter of VSC-MTDC system such as PLL bandwidth.

When the sensitivity is positive, it means that when the control parameter x increases, the eigenvalue magnitude increases, and vice versa.

The normalized sensitivities of the eigenvalue magnitude $|\lambda_k|$ to the control parameters are of much greater concern. The normalized sensitivity of the eigenvalue magnitude to the control parameter x is specifically expressed as:

$$S_x^{|\lambda_k(s)|} = \hat{S}_x^{\lambda_k(s)} \frac{x}{|\lambda_k(s)|} = \mathrm{Re}\left(S_x^{\lambda_k(s)}\right) \tag{40}$$

The larger the normalized sensitivity of eigenvalue magnitude, the greater the effect of control parameter on the eigenvalue.

Because this section mainly discusses the method of identifying the key factors by using the eigenvalues of the system open-loop gain matrix, the system eigenvalues in case I are selected as the object. In Fig. 5(b), only the eigenvalue λ_5 encircling the point $(-1,0)$ reflects the effect of the inverter-terminal VSCs on system stability and the characteristics between the inverter-terminal and the rectifier-terminal VSCs on system stability. Because λ_1-λ_4 do not encircle the point $(-1,0)$, the control parameters of the rectifier-terminal VSCs are reasonable. The AC grid and DC network consist of passive components, and there is no control loop. Therefore, λ_5 is mainly affected by the AC ports of the inverter-terminal VSCs. The system instability is mainly caused by the 3rd or 4th VSC. Because the control parameters and internal structures of the 3rd and 4th VSCs are the same. Only the SCR of the AC grid interconnected by the 3rd VSC is smaller than that by the 4th VSC. Therefore, it can be concluded that the port 3 of the 3rd VSC is the resonance interface based on the stability analysis laws, which says a single VSC is more likely to oscillate when connected to a weak grid [28], [29]. The 3rd VSC corresponding to the port 3 is the dominant resonant module [25]. Based on the effect of control parameters on stability of a single VSC [28], [29], the DC voltage control parameters, the PLL control parameters, and the sampling filtering period of the VSC are discussed and analyzed in detail. The normalized sensitivities of the eigenvalue magnitude to these control parameters are compared at f_0 in Table I.

TABLE I
Normalized Sensitivities of Eigenvalue Magnitude

Control parameter	$S_x^{\lvert\lambda_k(s)\rvert}$	Sensitivity symbol
k_{pv}	−1.9100	Positive
k_{iv}	0.1800	Negative
k_{pp}	−0.1700	Positive
k_{ip}	0.0800	Negative
T_s	−0.0043	Positive

In Table I, k_{pv} and k_{iv} represent the proportional and integral coefficients of DC voltage control, respectively; k_{pp} and k_{ip} represent the proportional and integral coefficients of PLL control, respectively; and T_s is the sampling filtering period. According to the result in Table I, the proportional coefficient of DC voltage control has the greatest impact on the eigenvalue magnitude. The sensitivities of the eigenvalue $|\lambda_5(f_0)|$ to k_{pv}, k_{pp}, and T_s are positive. With the increase of k_{pv}, k_{pp}, and T_s, the eigenvalue increases. The sensitivities of eigenvalue $|\lambda_5(f_0)|$ to k_{iv} and k_{ip} are negative. With the decrease of k_{iv} and k_{ip}, the eigenvalue increases. Therefore, the proportional coefficients of DC voltage control for the 3rd VSC can be preferentially increased to ensure the safe and stable operation of the system.

To intuitively reflect the effect of control parameters on eigenvalue, the frequency curves of eigenvalue λ_5 are shown in Fig. 9. In the corresponding frequency curve, $\mathrm{Im}[\lambda_5(f_0)] = 0$ and $\mathrm{Re}[\lambda_5(f_0)] < -1$. If the system is stable, the frequency curves of all eigenvalues satisfy $\mathrm{Im}[\lambda_k(f)] = 0$ and $\mathrm{Re}[\lambda_k(f)] > -1$. Therefore, $\mathrm{Re}[\lambda_5(f_0)]$ needs to be increased to greater than -1 at the frequency f_0.

The eigenvalues λ_1-λ_4 are only related to the control pa-

rameters of the 1st and 2nd VSCs. The control parameter transformation of the 3rd VSC does not affect the eigenvalues λ_1-λ_4. The Nyquist diagrams of eigenvalues λ_1-λ_4 and λ_6-λ_8 are shown in Appendix A Figs. A2 and A3, respectively, when the control parameters k_{pv}, k_{iv}, k_{pp}, k_{ip}, and T_s are increased by 1.1 times. It can be observed that as the control parameters change, the eigenvalues λ_1-λ_4 and λ_6-λ_8 do not encircle the point $(-1,0)$. Therefore, this paper only focuses on the sensitivities of λ_5 to the control parameters. To verify the above sensitivity analysis results, the frequency curves and Nyquist plots of eigenvalue λ_5 are shown in Fig. 10 when the control parameters k_{pv}, k_{iv}, k_{pp}, k_{ip}, and T_s are increased by 1.1 times.

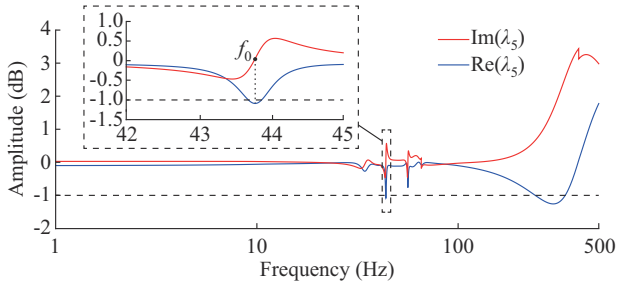

Fig. 9. Frequency curves of eigenvalue λ_5.

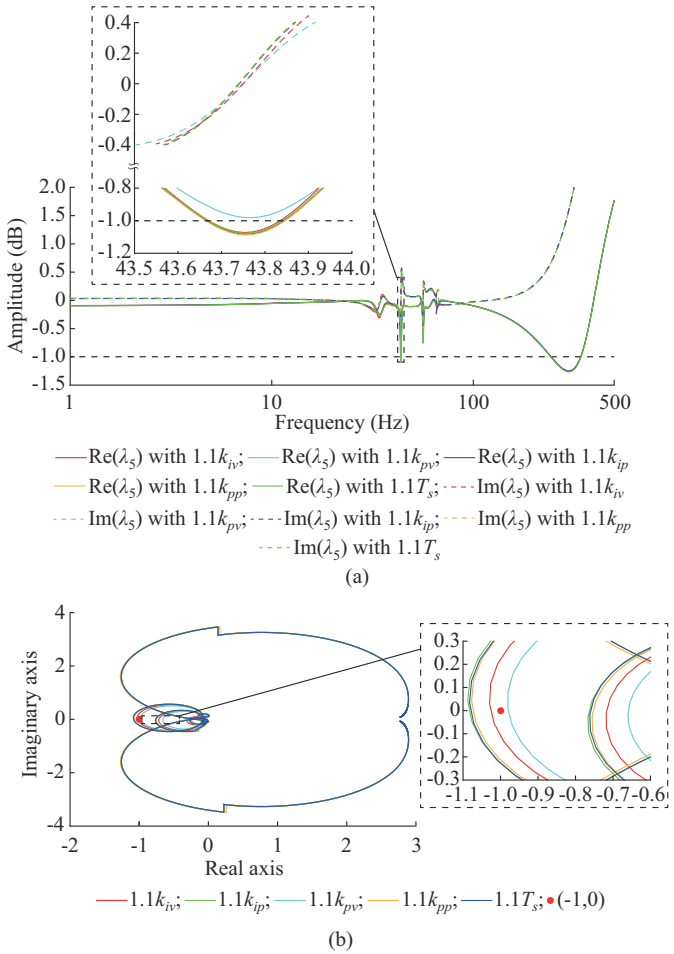

Fig. 10. Frequency curves and Nyquist plot of eigenvalue λ_5 with different control parameters. (a) Frequency curves. (b) Nyquist plot.

In Fig. 10(b), when the proportional coefficient of DC voltage control increases to $1.1k_{pv}$, the imaginary part of eigenvalue λ_5 changes little, and the real part of the eigenvalue λ_5 is greater than -1. The eigenvalue λ_5 does not encircle the point $(-1,0)$. The system is stable. This is in agreement with the simulation waveform of grid current in Fig. 11(a).

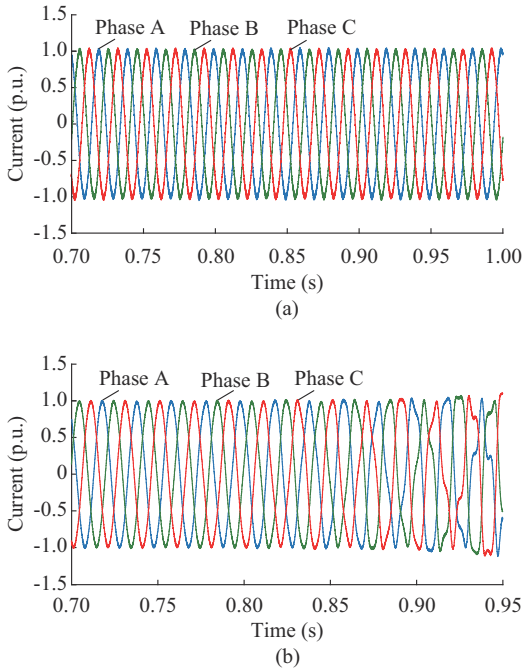

Fig. 11. Simulation waveforms of grid current with different control parameters. (a) $1.1k_{pv}$. (b) $1.1k_{pp}$.

When other parameters are increased by 1.1 times, the real parts of eigenvalue λ_5 change little. The eigenvalue λ_5 still encircles the point $(-1,0)$ and the system is unstable. The simulation waveform of grid current is shown in Fig. 11(b) when the proportional coefficient of PLL control increases to $1.1k_{pp}$. The simulation waveforms and the frequency curves of the eigenvalue λ_5 are consistent with the analysis results of the normalized sensitivities. Therefore, the dominant control parameter that affects the stability can be determined by comparing the normalized sensitivities of the eigenvalue magnitudes and parameters.

When k_{pv} changes, the frequency curves and Nyquist plots of the eigenvalue λ_5 are shown in Fig. 12.

When k_{pv} is increased by 1.1 times, the real part of the eigenvalue λ_5 increases. When the imaginary part the eigenvalue λ_5 is zero, the real part of the eigenvalue λ_5 is greater than -1, and the eigenvalue λ_5 does not encircle $(-1,0)$, which means that the system is stable. When k_{pv} is reduced by 0.9 times, the real part of eigenvalue λ_5 decreases. The eigenvalue λ_5 encircles the point $(-1,0)$ and the system is unstable.

Figure 13 shows the simulation waveform of grid current with $0.9k_{pv}$. The control parameters can be adjusted according to the positive and negative values of the eigenvalue and parameter sensitivity. This analysis conclusion is consistent with the simulation results.

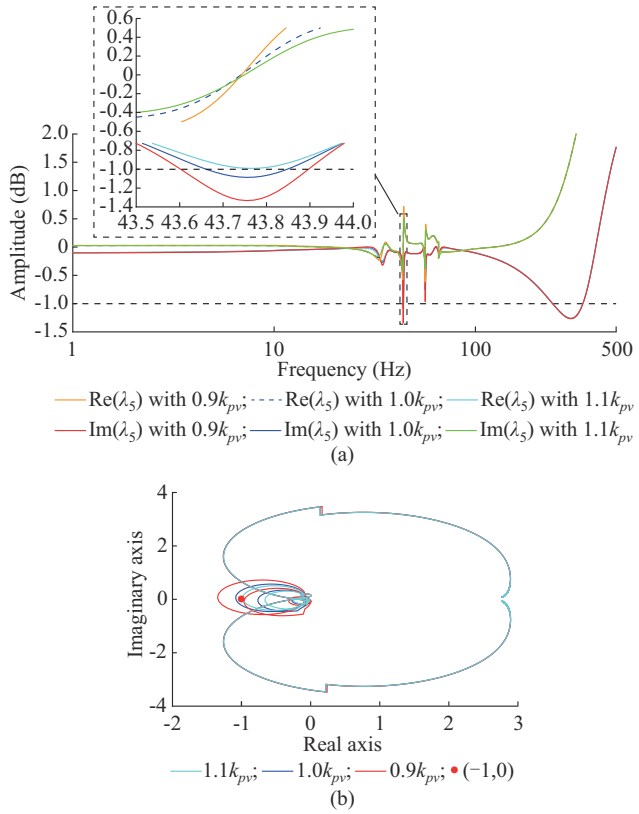

Fig. 12. Frequency curves and Nyquist plot of eigenvalue λ_5 with different k_{pv}. (a) Frequency curves. (b) Nyquist plot.

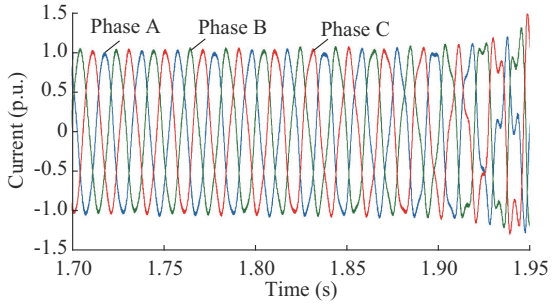

Fig. 13. Simulation waveforms of grid current with 0.9k_{pv}.

V. Conclusion

This paper proposes a multi-port network model of the VSC-MTDC system interconnecting AC grids with different SCRs and initial phases. The system stability and the key factors are analyzed based on the proposed multi-port network model. The analysis results are verified by simulation in MATLAB/Simulink. The main contributions and conclusions of this paper are summarized as follows.

1) The multi-port network model of VSC-MTDC system can be derived by multiplying the port transmission parameter matrices of the SSs, thus eliminating the need for iteration in the impedance model.

2) The port model of SSs considering the SSPs can improve the accuracy of the system stability analysis when the SCRs or the initial phases of the grids are different.

3) The real part of the system eigenvalue is sensitive to the proportional coefficient of the DC voltage control. The increase of the proportional coefficient reduces the real part of the eigenvalue and increases the risk of system instability.

In the future, the proposed multi-port network model will be used to study the stability of VSC-MTDC system under different network topologies. Additionally, we will discuss the MMC system stability and its corresponding key factors.

Appendix A

A. Control Block Diagram

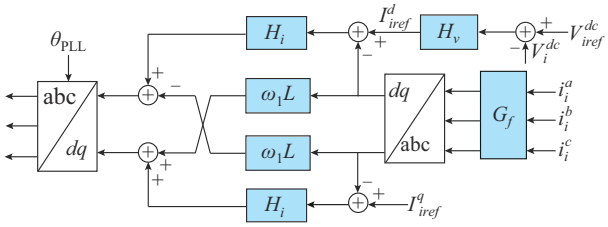

Fig. A1. Block diagram of DC voltage control for VSC.

TABLE AI
Parameters of VSC-MTDC System

Parameter	VSC1 and VSC2 (current control)	VSC3 and VSC4 (DC voltage control)
Rated AC voltage (kV)	110	110
Rated AC current (A)	1363	1363
Rated DC voltage (kV)	250	250
Rated power (MW)	150	150
DC filter capacitance (μF)	2000	2000

B. Effect of Control Parameters on Eigenvalues

When the control parameters of inverter are increased by 1.1 times, the Nyquist analysis diagrams of the eigenvalues λ_1-λ_4 and λ_6-λ_8 are shown in Fig. A2 and Fig. A3, respectively.

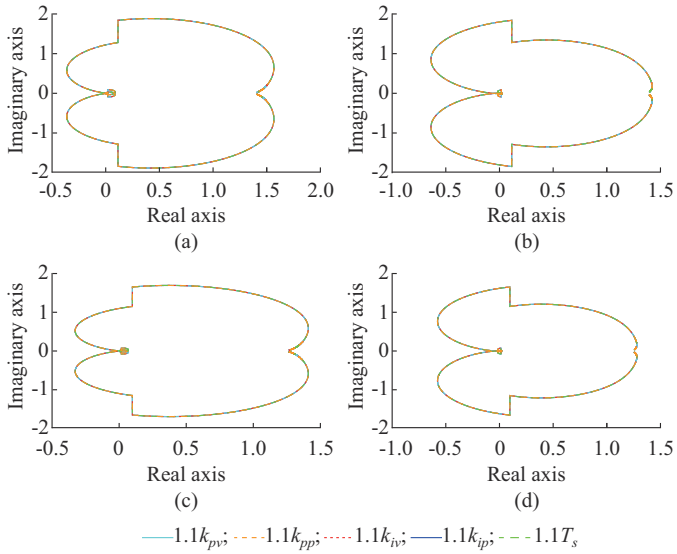

Fig. A2. Nyquist diagram of system eigenvalues. (a) λ_1. (b) λ_2. (c) λ_3. (d) λ_4.

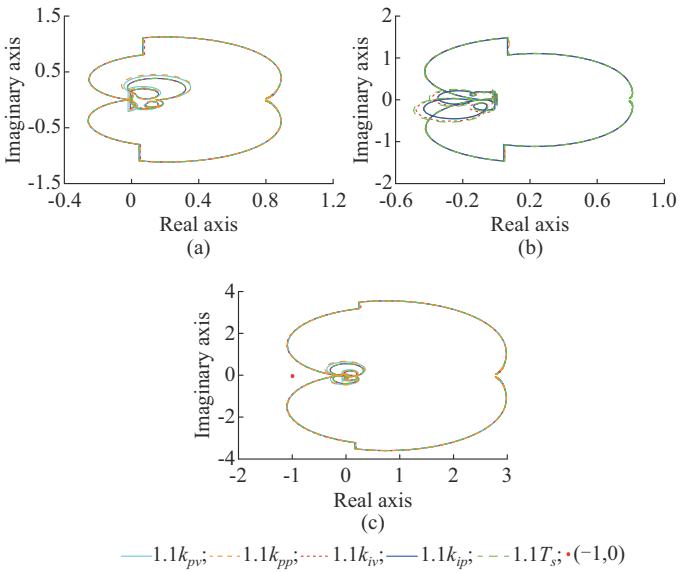

Fig. A3. Nyquist diagram of system eigenvalues. (a) λ_6. (b) λ_7. (c) λ_8.

REFERENCES

[1] C. Wang, W. Zheng, Z. Wang *et al*., "Partition-based network equivalent method for power system subsynchronous oscillation analysis," *Journal of Modern Power Systems and Clean Energy*, vol. 12, no. 1, pp. 313-320, Jan. 2024..

[2] Y. Meng, H. Wang, Z. Duan *et al*., "Small-signal stability analysis and improvement with phase-shift phase-locked loop based on back electromotive force observer for VSC-HVDC in weak grids," *Journal of Modern Power Systems and Clean Energy*, vol. 11, no. 3, pp. 980-989, May 2023.

[3] P. Chen, W. Zhao, X. Chen *et al*., "An impedance-based parameter design method for active damping of load converter station in MTDC distribution system," *Journal of Modern Power Systems and Clean Energy*, vol. 10, no. 5, pp. 1423-1436, Sept. 2022.

[4] L. Xu, L.Fan, and Z. Miao. "DC impedance model based resonance analysis of a VSC-HVDC system," *IEEE Transactions on Power Delivery*, vol 30, no. 3, pp. 1221-1230, Jun. 2015.

[5] Z. Huang, K. Wang, Y. Wang *et al*., "Small-signal stability constrained optimal power flow considering eigenvalue distribution," *Journal of Modern Power Systems and Clean Energy*, vol. 12, no. 4, pp. 1052-1062, Jul. 2024.

[6] G. O. Kalcon, G. P. Adam, O. Anaya-Lara *et al*., "Small-signal stability analysis of multi-terminal VSC-based DC transmission systems," *IEEE Transactions on Power Systems*, vol. 27, no. 4, pp. 1818-1830, Nov. 2012.

[7] J. Sun, "Two-port characterization and transfer immittances of AC-DC converters – Part I: modeling," *IEEE Open Journal of Power Electronics*, vol. 2, pp. 440-462, Aug. 2021.

[8] H. Xu, F. Nie, Z. Wang *et al*., "Impedance modeling and stability factor assessment of grid-connected converters based on linear active disturbance rejection control," *Journal of Modern Power Systems and Clean Energy*, vol. 9, no. 6, pp. 1327-1338, Nov. 2021.

[9] S.-F. Chou, X. Wang, and F. Blaabjerg, "Two-port network modeling and stability analysis of grid connected current controlled VSCs," *IEEE Transactions on Power Electronics*, vol. 35, no. 4, pp. 3519-3529, Apr. 2020.

[10] S. Shah and L. Parsa, "Impedance modeling of three-phase voltage source converters in *DQ*, sequence, and phasor domains," *IEEE Transactions on Energy Conversion*, vol. 32, no. 3, pp. 1139-1150, Sept. 2017.

[11] F. Ahmadloo and S. P. Azad, "Analysis of internal control loop interactions in VSCs: an individual design perspective," *IEEE Transactions on Power Delivery*, vol. 37, no. 3, pp. 1465-1475, Jun. 2022.

[12] X. Zou, X. Du, and G. Wang, "Modeling and stability analysis for multiple parallel grid-connected inverters system," in *Proceedings of 2018 IEEE Applied Power Electronics Conference and Exposition (APEC)*, San Antonio, USA, Mar. 2018, pp. 2431-2436.

[13] Y. Li, Z. Shuai, J. Fang *et al*., "Small-signal stability analysis method for hybrid AC-DC systems with multiple DC buses," *IEEE Journal on Emerging and Selected Topics in Circuits and Systems*, vol. 11, no. 1, pp. 17-27, Mar. 2021.

[14] D. Yang and Y. Sun, "SISO impedance-based stability analysis for system-level small-signal stability assessment of large-scale power electronics-dominated power systems," *IEEE Transactions on Sustainable Energy*, vol. 13, no. 1, pp. 537-550, Jan. 2022.

[15] S. Tan, X, Du, J. Liu *et al*., "Modeling and stability analysis of VSC-HVDC system considering AC/DC dynamic interaction response with frequency coupling," in *Proceedings of 2020 IEEE 9th International Power Electronics and Motion Control Conference*, Nanjing, China, Nov. 2020, pp. 2786-2792.

[16] J. Sun, "Two-port characterization and transfer immittances of AC-DC converters – Part II: applications," *IEEE Open Journal of Power Electronics*, vol. 2, pp. 483-510, Aug. 2021.

[17] L. Fan and Z. Miao, "Admittance-based stability analysis: bode plots, Nyquist diagrams or eigenvalue analysis?" *IEEE Transactions on Power Systems*, vol. 35, no. 4, pp. 3312-3315, Jul. 2020.

[18] C. Zhang, M. Molinas, A. Rygg *et al*., "Impedance-based analysis of interconnected power electronics systems: impedance network modeling and comparative studies of stability criteria," *IEEE Journal of Emerging and Selected Topics in Power Electronics*, vol. 8, no. 3, pp. 2520-2533, Sept. 2020.

[19] W. Cao, Y. Ma, and F. Wang, "Sequence-impedance-based harmonic stability analysis and controller parameter design of three-phase inverter-based multibus AC power systems," *IEEE Transactions on Power Electronics*, vol. 32, no. 10, pp. 7674-7693, Oct. 2017.

[20] G. Qiu. *Circuit*. Beijing: Higher Education Press, 2006.

[21] J. Pedra, L. Sainz, and L. Monjo, "Three-port small signal admittance-based model of VSCs for studies of multi-terminal HVDC hybrid AC/DC transmission grids," *IEEE Transactions on Power Systems*, vol. 36, no. 1, pp. 732-743, Jan. 2021.

[22] H. Zhang, M. Mehrabankhomartash, M. Saeedifard *et al*., "Impedance analysis and stabilization of point-to-point HVDC systems based on a hybrid AC/DC impedance model," *IEEE Transactions on Industrial Electronics*, vol. 68, no. 4, pp. 3224-3238, Apr. 2021.

[23] J. Sun and H. Liu, "Sequence impedance modeling of modular multilevel converters," *IEEE Journal of Emerging and Selected Topics in Power Electronics*, vol. 5, no. 4, pp. 1427-1443, Dec. 2017.

[24] X. Wang, L. Harnefors, and F. Blaabjerg, "Unified impedance model of grid-connected voltage-source converters," *IEEE Transactions on Power Electronics*, vol. 33, no. 2, pp. 1775-1787, Feb. 2018.

[25] H. Zhang, X. Wang, M. Mehrabankhomartash *et al*., "Harmonic stability assessment of multiterminal DC (MTDC) systems based on the hybrid AC/DC admittance model and determinant-based GNC," *IEEE Transactions on Power Electronics*, vol. 37, no. 2, pp. 1653-1665, Feb. 2022.

[26] L. Wang, X. Xie, J. Shair *et al*., "Frequency-domain admittance network model (FANM) based oscillatory stability analysis of hybrid AC-DC systems with MMCs," *IEEE Transactions on Power Systems*, vol. 39, no. 2, pp. 3444-3458, Mar. 2024

[27] E. Chung, G. C. Lim, J.-I. Ha *et al*., "Resonant converter design using two-port passive network: single frequency design," in *Proceedings of COMPEL Workshop*, Padova, Italy, Jun. 2018, pp. 1-7.

[28] Q. Chen, S. Bu, and C. Y. Chung, "Small-signal stability criteria in power electronics-dominated power systems: a comparative review," *Journal of Modern Power Systems and Clean Energy*, vol. 12, no. 4, pp. 1003-1018, Jul. 2024.

[29] B. Wen, D. Boroyevich, R. Burgos *et al*., "Analysis of *D-Q* small-signal impedance of grid-tied inverters," *IEEE Transactions on Power Electronics*, vol. 31, no. 1, pp. 675-687, Jan. 2016.

Shangning Tan received the B.S. degree in electrical engineering and automation from Northwest A&F University, Xi'an, China, in 2016. She is currently pursuing the Ph.D. degree in power electronics engineering in Power Electronics Engineering, Chongqing University, Chongqing, China. Her research interests include modeling, stability analysis, and control of power systems based on power electronics.

Junliang Liu received the B.S. degree in electrical engineering and automation from Linyi University, Linyi, China, in 2015, the M.S. degree in control engineering from the Chongqing University of Posts and Telecommunications, Chongqing, China, in 2018, and the Ph.D. degree in electrical engineering from Chongqing University, Chongqing, China, in 2022. He is currently a Research Associate with the School of Electrical Engineering, Chongqing University. His research interest includes stability of power elec-

tronics system.

Xiong Du received the B.S., M.S., and Ph.D. degrees from Chongqing University, Chongqing, China, in 2000, 2002, and 2005, respectively, all in electrical engineering. Since 2002, he has been with Chongqing University, where he is currently a Full Professor with the School of Electrical Engineering. He was a Visiting Scholar with Rensselaer Polytechnic Institute, Troy, USA, from 2007 to 2008. His research interests include reliability and stability of power electronics system.

Jingyuan Su received the B.Eng. degree in electrical engineering and automation and Ph.D. degree in electric engineering from the Huazhong University of Science and Technology, Wuhan, China, in 2014 and 2020, respectively. She is currently a Postdoctoral Research Scholar with the School of Electrical Engineering, Chongqing University, Chongqing, China. Her research interests include brushless doubly fed generation, parameter estimation, and power electronics.

Lijuan Fan received the B.S. and M.S. degrees from Tsinghua University, Beijing, China, in 2006 and 2009, respectively. She is currently in China Southern Power Grid Research Institute Co., Ltd., Guangzhou, China. Her research interests include power system calculation analysis and DC transmission technology research.